Journal of Catalysis 282 (2011) 94–102

Contents lists available at ScienceDirect

Journal of Catalysis

journal homepage: www.elsevier.com/locate/jcat

Au/TiO_2@SBA-15 nanocomposites as catalysts for direct propylene epoxidation with O_2 and H_2 mixtures

Chun-Hsia Liu [a], Yejun Guan [b], Emiel J.M. Hensen [b], Jyh-Fu Lee [c], Chia-Min Yang [a,*]

[a] Department of Chemistry, National Tsing Hua University, Hsinchu 30013, Taiwan
[b] Schuit Institute of Catalysis, Eindhoven University of Technology, P.O. Box 513, 5600 MB Eindhoven, The Netherlands
[c] National Synchrotron Radiation Research Center, Hsinchu 30076, Taiwan

ARTICLE INFO

Article history:
Received 9 April 2011
Revised 29 May 2011
Accepted 1 June 2011
Available online 5 July 2011

Keywords:
Gold catalyst
Propylene epoxidation
Mesoporous material
Nanocomposite
Selective deposition

ABSTRACT

A nanostructured Au/TiO_2@SBA-15 catalyst has been prepared and applied in propylene epoxidation with a mixture of O_2/H_2. The mesopores of SBA-15 were first deactivated by grafting of hydrophobic groups. Titanium was then selectively grafted in the micropores of SBA-15 by reaction with titanium isopropoxide followed by calcination and deposition of Au nanoparticles. The nanocomposite catalysts exhibited relatively stable propylene oxide (PO) production with small amounts of propanal and acetone byproducts. A catalyst prepared by grafting with trimethylsilyl groups, a Ti/Si ratio of 0.05 and very small Au nanoparticles (<2 nm), showed the highest catalytic activity. The improved performance appears to be related to the interaction of very small Au nanoparticles in close contact with very small sized TiO_2 domains in combination with the hydrophobicity of the fully open mesopores. The results demonstrate the possibility to improve the catalytic performance of Au–Ti catalysts through rational catalyst design.

1. Introduction

Propylene oxide (PO) is an important chemical intermediate for the production of a variety of chemicals and polymers [1]. Commercially, PO is produced via the chlorohydrin process and several hydroperoxide processes [2]. However, the chlorohydrin process results in large amounts of chlorinated compounds, and the hydroperoxide processes typically generate stoichiometric quantities of coproducts. Several companies including Dow and BASF have recently developed liquid-phase propylene epoxidation processes catalyzed by titanium silicalite-1 (TS-1) using hydrogen peroxide as the oxidant [3–6], but the processes incur the cost associated with the use of H_2O_2. Following the success of ethylene epoxidation by silver-based catalysts [7–9], direct gas-phase propylene epoxidation using molecular oxygen has also been extensively studied. The PO selectivities are very poor for silver [10–12] and copper [13,14] catalysts due to the higher reactivity of propylene as compared to ethylene. The development of gold-based catalysts supported on titania (TiO_2) or titanium-modified surfaces has been a promising research direction in recent years [15–19]. The direct propylene epoxidation by oxygen over gold-based catalysts needs hydrogen to activate oxygen under milder conditions [20], and the reactions may produce a variety of byproducts including water, carbon dioxide (the product of complete combustion), acrolein (the product of oxidation instead of epoxidation), and other hydrocarbons that result from the hydrogenation of propylene (propane), isomerization (e.g. propanal and acetone) and cracking (e.g. ethanal) of the final product [21–23]. Although Au–Ti catalysts are generally very selective (>90%), they still suffer from low propylene conversion, low hydrogen efficiency, and poor catalyst stability that need to be improved to meet the requirements (10% propylene conversion, 90% PO selectivity, and 30% hydrogen efficiency) for large-scale industrial process [16–19].

For the direct propylene epoxidation over Au–Ti catalysts, it is generally agreed that the primary role of Au is to produce peroxide species to epoxidize propylene over a Ti site [16–19,24–28] and that the size of Au particles and the nature of the titanium-containing supports are decisive to the activity of the catalysts. By using bulk TiO_2 as supports, Haruta et al. found that 2- to 5-nm Au nanoparticles are preferred for PO production. Smaller Au nanoparticles catalyze propane formation, and larger particles lead to an increase in the rate of full combustion [15]. They also found that anatase-supported catalysts give high PO selectivity but lead to fast deactivation and low PO yields, whereas rutile or amorphous TiO_2-supported catalysts result in complete combustion to CO_2 [29].

In addition, the presence of the tetrahedral-coordinated Ti sites is crucial for catalytic activity. Tetrahedral-coordinated Ti sites are involved in the adsorption of propylene [17,30]. They may serve as nucleation sites for Au nanoparticles [31] and may even probably alter the electronic structure of Au [32]. However, these sites, together with neighboring surface hydroxyl (Ti–OH or Si–OH)

* Corresponding author. Fax: +886 3 5165521.
E-mail address: cmyang@mx.nthu.edu.tw (C.-M. Yang).

0021-9517/$ - see front matter © 2011 Elsevier Inc. All rights reserved.
doi:10.1016/j.jcat.2011.06.001

groups, may also involve in the readsorption of the PO molecules [33], which further causes catalyst deactivation by producing bidentate propoxy species, carbonates, carboxylates, and oligomers on catalyst surface [16–19,33–36]. Isolated or at least highly dispersed tetrahedral Ti sites supported on high-surface-area supports, such as mesoporous silicas [37], may therefore stabilize catalyst performance. Indeed, gold nanoparticles on Ti-modified MCM-41, MCM-48, TUD-1, and SBA-15 silicas make good catalysts with improved PO yields [21,38–44]. However, the activity loss with time on stream is still a serious issue. The hydrophobization of the Au–Ti catalysts supported on MCM-41 and MCM-48 improved propylene conversion, hydrogen efficiency, and catalyst stability [21,44], but even the silylated catalysts underwent about 35–40% activity loss after 4 h time on stream [44]. The addition of water to the feed gas was shown to suppress deactivation [45], but it also caused a decrease in the catalytic activity.

Clearly, there is considerable scope for further improvement in gold catalysts for PO production. Here, we report a new type of Au/TiO_2@SBA-15 catalysts that make use of the bimodal pore arrangement of SBA-15 silica [46,47]. Our approach is exemplified in Scheme 1. The mesopores of SBA-15 were first grafted with hydrophobic trimethylsilyl (TMS) or triphenylsilyl (TPS) groups [48,49]. The micropores were subsequently vacated and functionalized by grafting with Ti(iOPr)$_4$ at different loadings. Finally, gold was introduced by a standard method. The intermediate and final Au/TiO_2@SBA-15 materials were thoroughly characterized by nuclear magnetic resonance (NMR) spectroscopy, inductively coupled plasma-mass spectroscopy (ICP-MS), N_2 physisorption, X-ray diffraction (XRD), X-ray absorption spectroscopy (XAS), and transmission electron microscopy (TEM). When tested for the direct propylene epoxidation with O_2/H_2, most of the Au/TiO_2@SBA-15 catalysts showed marginally better but more stable activities as compared to the reported Au/Ti-SBA-15 [41,42] and some other mesoporous silica-based Au–Ti catalysts [21,40]. More interestingly, all the Au/TiO_2@SBA-15 catalysts only produced water and small amounts of isomerization byproducts (i.e. propanal and acetone) in addition to the main product PO. Furthermore, we found that the most active catalyst had the smallest Au nanoparticles among all the Au/TiO_2@SBA-15 catalysts, and its high catalytic activity is most likely due to the very small size of Au in it. The relation of the structural properties of the nanocomposites to the catalytic performance will be discussed.

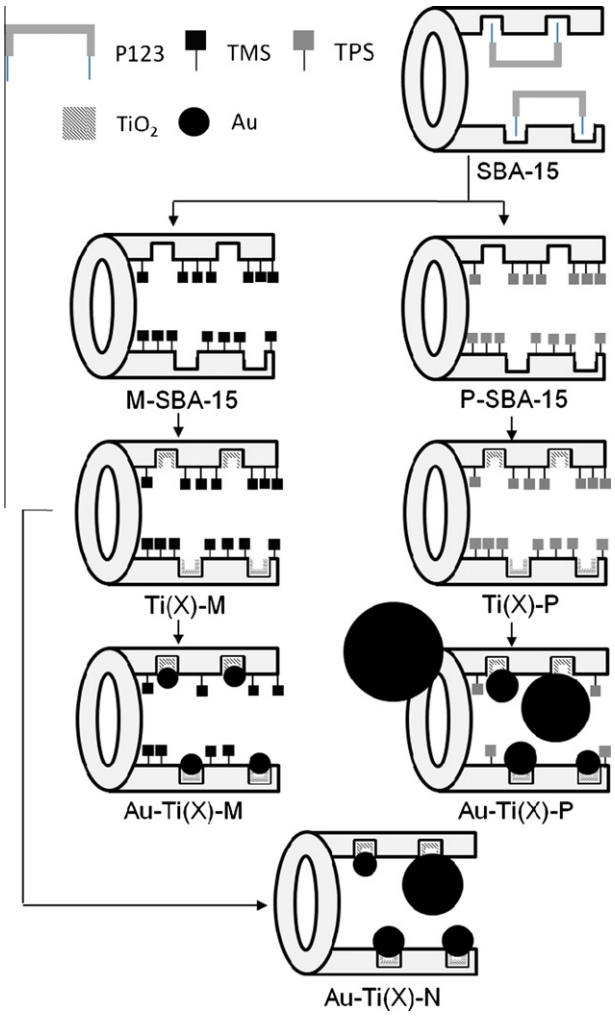

Scheme 1. Schematic representation of the preparation of functionalized SBA-15 and Au/TiO_2@SBA-15 nanocomposites.

2. Experimental

2.1. Catalyst preparation

Mesoporous SBA-15 silica was synthesized by adding tetraethoxysilane (TEOS) to a HCl solution of Pluronic P-123 (EO20PO70EO20), resulting in a mixture with a molar composition of 1 TEOS:0.017 P-123:0.54 HCl:100 H_2O. The mixture was stirred at 35 °C for 24 h and further aged at 60 °C for 24 h. The product was filtered and dried at 90 °C. The mesopores of SBA-15 were selectively vacated by stirring the as-synthesized SBA-15 in 45 wt.% H_2SO_4 solution at 95 °C for 24 h [50,51]. The open mesopores in the acid-treated SBA-15 were grafted with TMS or TPS groups. For the grafting with TMS groups [48,49], the dried acid-treated SBA-15 was poured into a toluene solution of trimethylchlorosilane (TMCS) and stirred at room temperature for 0.5 h. Alternatively, the dried silica sample was refluxed in a pyridine solution of triphenylchlorosilane (TPCS) at 120 °C for 24 h to be grafted with TPS groups. Subsequently, the micropores of the materials were vacated by a thermal treatment at 250 °C in air, resulting in samples referred to as M-SBA-15 (grafted with TMS groups) and P-SBA-15 (grafted with TPS groups) (cf. Scheme 1).

For the incorporation of Ti with different titanium-to-silicon (Ti/Si) molar ratios, the functionalized SBA-15 samples were evacuated and heated at 200 °C for 6 h and then impregnated with calculated amounts of titanium isopropoxide in dry isopropanol. The impregnated samples were dried under flowing nitrogen at room temperature for 48 h and then heated to 350 °C in air for 0.5 h. The TiO_2-incorporated samples are referred to as Ti(x)-Y, where x denotes the target Ti/Si ratio (x = 0.01, 0.05, and 0.10) and Y denotes the type of grafted hydrophobic groups (with Y being M or P for TMS- or TPS-grafted samples, respectively). For the purpose of comparison, a portion of the Ti(x)-M samples was further heated at 450 °C in air for 3 h to completely decompose the hydrophobic groups. These samples are designated as Ti(x)-N.

Gold particles were deposited on the TiO_2-incorporated samples by a deposition–precipitation method using an aqueous solution of $HAuCl_4$ and NaOH as the precipitant. In a typical preparation, an aqueous solution of $HAuCl_4$ (0.17 g $HAuCl_4{\cdot}4H_2O$ in 50 mL water) was first prepared at room temperature followed by adjustment of the solution pH to 7.0 using aqueous NaOH [52]. The TiO_2-incorporated support (0.5 g) was immersed in a small amount of acetone followed by suspension in water (50 mL) and adjustment of the solution pH to 7.0. The $HAuCl_4$ solution was then added to the stirred suspension at 35 °C. The solution pH was again adjusted and kept at 7.0, and the mixture was stirred for 2 h before the product was filtered, washed, dried in air at 90 °C overnight, and

calcined in air at 400 °C for 4 h. The resulting Au/TiO_2@SBA-15 nanocomposites are referred to as Au–Ti(x)-Y.

2.2. Catalyst characterization

Solid-state NMR spectra were measured on a Bruker DSX400WB spectrometer using 4-mm MAS probes at a spinning rate of 6.5 kHz. XRD patterns were obtained on a Mac Science 18MPX diffractometer using Cu K_α radiation. The ICP-MS data were obtained using a Perkin-Elmer SCIEX-ELAN 5000 device. Ti K-edge and Au L_3-edge XAS measurements were taken on the beamlines 01C and 17C at the National Synchrotron Radiation Research Center (NSRRC, Taiwan) with a storage ring energy of 1.5 GeV. For the Ti K-edge measurements, the samples were dehydrated at 300 °C in flowing nitrogen for 1 h. In a typical XAS experiment, about 100 mg of sample was pressed to form self-supporting wafers before being mounted in a cell for measurements. Measurements were taken at room temperature in normal step scanning mode, and multiple scans were obtained to improve the signal-to-noise ratio. N_2 physisorption isotherms were measured at 77 K using a Quantachrome Autosorb-1-MP instrument. The isotherms were analyzed by the nonlocal density functional theory (NLDFT) method to evaluate pore sizes of the samples using the kernel of NLDFT equilibrium capillary condensation isotherms of nitrogen at 77 K on silica (adsorption branch, assuming cylindrical pore geometry). The BET surface areas were calculated from the adsorption branches in the relative pressure range of 0.05–0.30, and the total pore volumes were evaluated at a relative pressure of 0.95. TEM images were taken on a FEI Tecnai 20 electron microscope operated at 200 kV and a field-emission JEOL JEM-3000F electron microscope operated at 300 kV and equipped with a high-angle annular dark field (HAADF) detector and an energy dispersion spectrometer (EDS).

2.3. Catalyst activity measurements

Catalytic activity was measured in a fixed-bed flow reactor using 0.1 g of the prepared catalyst and a feed consisting of 10 vol.% propylene, 10 vol.% O_2, and 10 vol.% H_2 in He at a flow rate of 25 mL min^{-1}. This corresponds to a space velocity of 15,000 $cm^3\ h^{-1}\ g_{cat}^{-1}$ based on total flow. The reactor was placed in a tubular furnace, and the gas feed was preheated before passing over the catalyst. The reactor effluent was analyzed every 5.5 min using an Interscience Compact gas chromatography system, equipped with Molsieve 5A and Porabond Q columns, each equipped with a thermal conductivity detector (TCD). After measurements at a reaction temperature (80 °C, 120 °C, and 150 °C) for 4 h, the catalyst was regenerated by heating at 300 °C for 1 h in 10 vol.% O_2 in He before proceeding to the next reaction temperature.

3. Results and discussion

3.1. Solid-state NMR measurements

The stepwise removal of the P-123 template and the grafting of the TMS or TPS groups on the mesopores of SBA-15 were monitored by solid-state ^{13}C CP/MAS and ^{29}Si MAS NMR and gave similar results as reported before [48–51]. Fig. 1 shows the ^{29}Si NMR spectra of M-SBA-15 and P-SBA-15. Their spectra exhibit the Q lines (Q^n: $Si(OSi)_n(OH)_{4-n}$, n = 2–4) attributed to the SBA-15 silica support. The additional silicon atoms of the functional groups give rise to the T lines in the spectra, *i.e.* at 14 and −18 ppm for TMS and TPS, respectively. The intensity ratios of the T and Q lines for the two samples are around 9:100. Some of the functional groups were decomposed during Ti incorporation, as evidenced by less intense T lines. For example, the T/Q intensity ratios for Ti(0.01)-M and Ti(0.01)-P are decreased to 7:100 and 6:100, respectively (cf. Fig. 1), upon Ti incorporation. Subsequent steps of deposition and activation of Au nanoparticles resulted in further loss of these groups. The T/Q ratio for Au–Ti(0.01)-M is about 3:100, corresponding to ~60% loss of the TMS groups originally in M-SBA-15. For Au–Ti(0.01)-P, no discernable T lines were observed, and thus nearly all the TPS groups were decomposed . Other samples with higher titania content also showed similar trends in the loss of the functional groups.

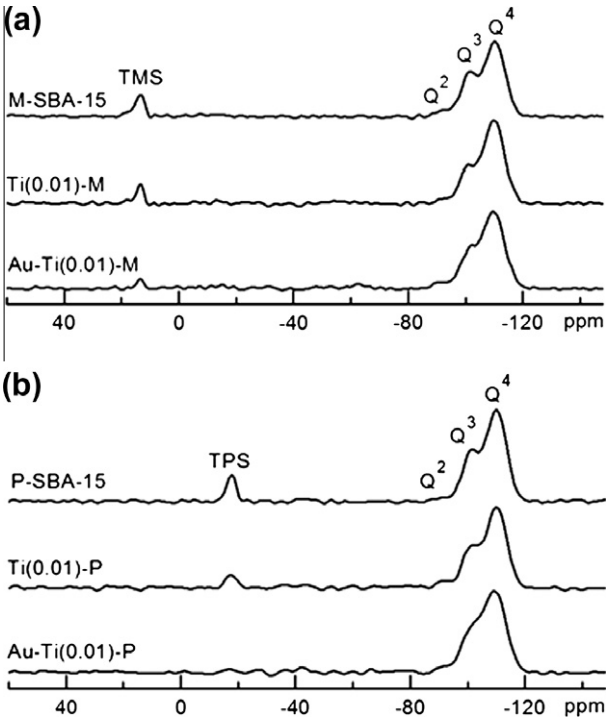

Fig. 1. ^{29}Si MAS NMR spectra of selected samples functionalized with (a) TMS and (b) TPS groups.

3.2. Elemental analysis

The elemental composition of the Au/TiO_2@SBA-15 materials, as determined by ICP-MS, is given in Table 1. The Ti/Si ratios for all samples are very close to the target loadings. Concerning the Au loading, Au–Ti(x)-M and Au–Ti(x)-P were expected to have similar loadings, because the mesopore surface was still covered by TMS or TPS groups during the deposition. We expect that the Au nanoparticles were deposited on the TiO_2 nanophases. However, the Au loadings in Au–Ti(x)-P (0.70–1.02 wt.%) are significantly higher than those in Au–Ti(x)-M (0.16–0.25 wt.%). This is probably related to the weak π-cation interactions between Au^{3+} and the benzene rings of the TPS groups [53], which may increase the amount of Au deposited on the hydrophobic part of the TPS-functionalized sample. For Au–Ti(x)-N, the TMS groups were thermally decomposed prior to Au deposition onto the exposed titania/silica surfaces and the Au loadings varies considerably (0.06–0.45 wt.%).

3.3. Textural properties

The N_2 physisorption measurements evidence that most of the Au/TiO_2@SBA-15 materials have fully open mesopores. Fig. 2 shows the isotherms of functionalized SBA-15 and the Au/TiO_2@SBA-15 samples with maximum titania loadings. The isotherms of M-SBA-15 and P-SBA-15 are type IV and exhibit sharp steps with

Table 1
Structural properties of functionalized SBA-15 and Au/TiO_2@SBA-15 samples.[a]

Sample	a (nm)	d (nm)	S_{BET} (m^2g^{-1})	V_t (cm^3g^{-1})	Ti/Si	w_{Au} (wt.%)	D_{Au} (nm)	CN_{Au-Au}
M-SBA-15	11.9	7.6	735	1.11	NA[b]	NA	NA	NA
P-SBA-15	11.9	7.3	760	1.08	NA	NA	NA	NA
Au–Ti(0.01)-M	10.8	7.6	662	1.07	0.013	0.16	NA	8.2
Au–Ti(0.05)-M	10.8	7.6	638	1.07	0.055	0.25	NA	6.6
Au–Ti(0.10)-M	10.8	7.6	625	1.05	0.101	0.17	NA	8.3
Au–Ti(0.01)-P	11.0	7.6	548	0.93	0.012	0.70	5–11	9.4
Au–Ti(0.05)-P	11.0	7.6	539	0.92	0.056	1.02	7–12	9.7
Au–Ti(0.10)-P	10.8	7.6	535	0.88	0.112	0.72	3–10	9.2
Au–Ti(0.01)-N	10.6	7.6	616	1.04	0.012	0.06	NA	NA
Au–Ti(0.05)-N	10.4	7.6	606	1.01	0.052	0.32	3–6	9.4
Au–Ti(0.10)-N	10.6	7.6	594	1.02	0.100	0.45	3–6	9.3

[a] a: cell constant; d: mesopore diameter; S_{BET}: BET surface area; V_t: total pore volume; w_{Au}: Au loading; D_{Au}: Au particle sizes observed by TEM; CN_{Au-Au}: Au–Au coordination number derived from EXAFS.
[b] Not applicable.

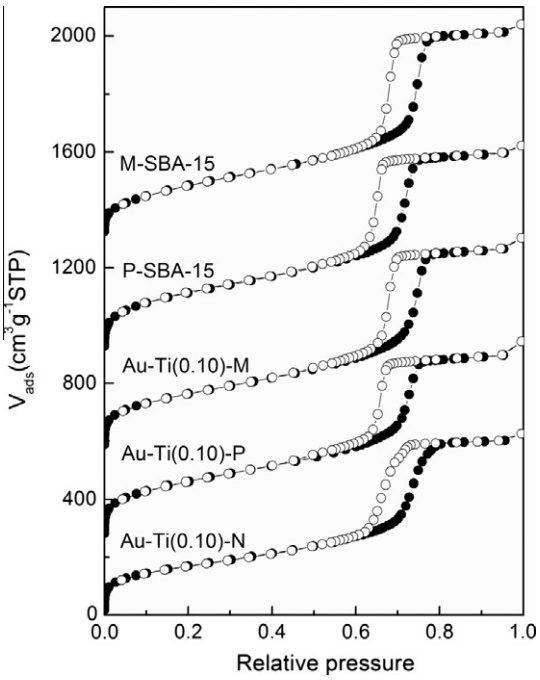

Fig. 2. N_2 physisorption isotherms of functionalized SBA-15 and Au–Ti(0.10)-Y samples. The isotherms are shifted by (from bottom to top) 0, 250, 560, 900, and 1300 $cm^3\ g^{-1}$ STP, respectively.

hysteresis loops corresponding to the filling of the ordered channel-type mesopores. The hysteresis loop for P-SBA-15 is slightly shifted to lower relative pressure as compared to the one for M-SBA-15, indicating that the diameter (7.3 nm) for P-SBA-15 grafted with TPS groups is slightly smaller than that (7.6 nm) for M-SBA-15 grafted with the somewhat smaller TMS groups. After Ti incorporation, the Ti(x)-M and Ti(x)-P samples gave almost identical isotherms with sharp steps (data not shown), suggesting that the TiO_2 nanophases should be preferentially incorporated in the micropores of SBA-15, because the hydrophobic TMS or TPS groups passivated the external and mesopore surfaces of SBA-15. These observations are consistent with our previous studies on the selective deposition of iron oxide and palladium nanoparticles in the micropores of SBA-15 [48,49]. On the other hand, further deposition of Au resulted in nanocomposites exhibiting distinct sorption behavior. Taking those with the highest Ti/Si ratio as examples, although the isotherms of Au–Ti(0.10)-M and Au–Ti(0.10)-P still exhibit sharp steps, Au–Ti(0.10)-P shows a larger reduction (~18%) in the total pore volume than Au–Ti(0.10)-M does (~5%) as compared to the parent functionalized SBA-15. It suggests that (i) the Au nanoparticles in Au–Ti(0.10)-M must be very small, and (ii) some of the channel-type mesopores in Au–Ti(0.10)-P are blocked, probably by Au nanoparticles with sizes comparable to the diameter of the mesopores. For Au–Ti(0.10)-N, the less sharp step in its isotherm suggests that the mesopores are slightly clogged, probably by some Au nanoparticles slightly larger than those in Au–Ti(0.10)-M.

3.4. X-ray diffraction

The ordered mesostructure and pore arrangement of SBA-15 remained intact in the surface-functionalized SBA-15 and all the Au/TiO_2@SBA-15 materials. The small-angle XRD patterns of the TMS- and TPS-functionalized SBA-15 and the Au/TiO_2@SBA-15 materials derived from TMS-functionalized SBA-15 (Au–Ti(x)-M) (Fig. S1 in the Supporting Material) exhibit typical reflections attributed to the hexagonal $p6mm$ structure, and the derived unit cell constants a are listed in Table 1. The ordered mesostructure of SBA-15 was not affected during the course of selective functionalization, but subsequent incorporation of TiO_2 and Au involving thermal treatments at 350–400 °C resulted in structural shrinkage (~8%) of the SBA-15 host. The wide-angle XRD patterns of the Au/TiO_2@SBA-15 samples (Fig. S2 in the Supporting Material) only showed a broad background attributed to amorphous silica except for TPS-functionalized Au–Ti(x)-P that also contained a reflection of Au. The XRD data show that (i) the TiO_2 nanophases in the micropores of all the materials are amorphous in nature or at least highly dispersed, (ii) all the Au nanoparticles in Au–Ti(x)-M and Au–Ti(x)-N must be very small, and (iii) Au–Ti(x)-P samples contain larger Au nanoparticles. The particle size in the latter samples is around 7–8 nm, which suggests that these are predominantly located in the channel-type mesopores of quite similar dimensions. This explains the observed reduction in the total pore volume for Au–Ti(x)-P (especially Au–Ti(0.10)-P). The formation of these Au nanoparticles may be attributed to their relatively high Au loadings and the stabilizing effects of the TPS groups for the Au nanoparticles through weak π–$Au^{(0)}$ interactions [53,54]. However, it should be mentioned that XRD data cannot exclude the possibility that also very small Au nanoparticles are present in Au–Ti(x)-P (see the section of Au XAS analysis).

3.5. Ti K-edge X-ray absorption spectroscopy

The local coordination of Ti^{4+} was studied by XAS, and the normalized X-ray absorption near-edge structure (XANES) spectra at Ti K-edge are shown in Fig. 3. It has been shown that the pre-edge peak is consistently positioned at 4969.2 eV with varied peak

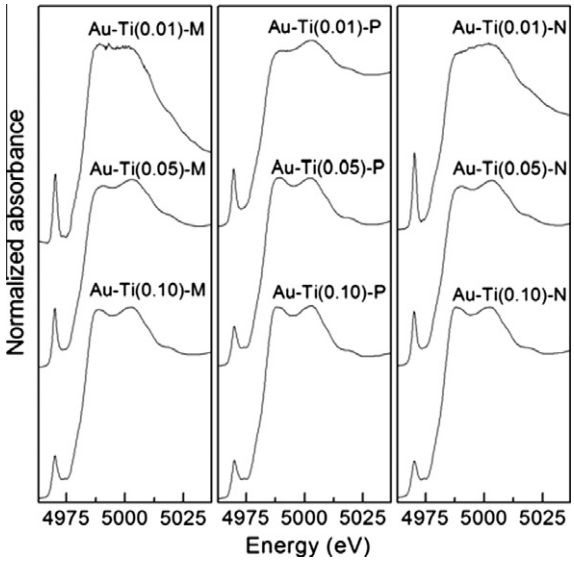

Fig. 3. Normalized Ti *K*-edge XANES spectra of the Au/TiO_2@SBA-15 samples.

intensity for the tetrahedrally coordinated Ti^{4+} in or on a silica matrix (e.g.TS-1) [41,55]. For TiAPO-5 and Ti-MCM-41 containing predominantly octahedral Ti^{4+}, however, the pre-edge peak is at around 4970.5 eV [55,56]. In Fig. 3, each spectrum exhibits a pre-edge peak at 4970.0 eV due to the 1s–3d transition, and the peak intensity decreases with increasing the Ti/Si ratio. It suggests that all the Au/TiO_2@SBA-15 materials contain a mixture of tetrahedral and higher (five and six) coordinated titanium species with varied relative amounts. The XANES result together with the data of N_2 physisorption and wide-angle XRD implicates that the titanium species in Au/TiO_2@SBA-15 are "aggregated" to form XRD-amorphous TiO_2 nanophases in the micropores of the host SBA-15.

3.6. Transmission electron microscopy

The TEM observations are consistent with the results of XRD and N_2 physisorption. Fig. 4 shows the TEM images of the representative samples with Ti/Si = 0.05. For Au–Ti(0.05)-M, the hexagonally arranged channel-type mesopores can be clearly seen, but no Au nanoparticles were observed. This sample was also measured by HAADF-STEM equipped with an EDS detector, but no discrete TiO_2 or Au nanoparticles could be clearly observed, although the EDS data confirmed the presence of Ti and Au (cf. Fig. S3 in the Supporting Materials). Probably, the Au and Ti content is too low to clearly image these nanoparticles. The pictures are similar for other Au–Ti(*x*)-M samples, suggesting that gold is highly dispersed in these materials. On the other hand, a few Au nanoparticles with sizes of about 7–12 nm are present in the mesopores and at the external surface of the silica support in Au–Ti(0.05)-P. For Au–Ti(0.05)-N, one could discern some dark spots in the TEM image as Au nanoparticles that are 3–6 nm in size and are distributed in the material. The average sizes of the Au nanoparticles observed in the TEM images for Au–Ti(*x*)-P and Au–Ti(*x*)-N (except Au–Ti(0.01)-N) are listed in Table 1.

3.7. Au L_3-edge X-ray absorption spectroscopy

The edge region of the Au L_3-edge XAS measurements has the absorption edge at 11,919 eV for all the Au/TiO_2@SBA-15 samples, indicating that the deposited Au precursors were fully reduced to form metallic Au^0 nanoparticles (Fig. S4 in the Supporting Material). The extended X-ray absorption fine structure (EXAFS) part was further analyzed, and the Fourier transform (FT) profiles of the k^3-weighted EXAFS data and the curve fitting results of selected samples are shown in Fig. 5. All the FT profiles mainly consist of a relatively broad first-shell peak corresponding to the nearest-neighbor Au–Au distance (d_{Au-Au}, or the Au–Au bond length). All the three Au–Ti(*x*)-M samples have nearly the same d_{Au-Au} of 2.80 Å, while the values for Au–Ti(0.05)-P and Au–Ti(0.05)-N are around 2.83 Å. Compared to the d_{Au-Au} value of 2.86 Å for the Au foil, the observed reduction in the Au–Au bond length can be explained by the contraction of the lattice due to the high surface energy of nanoparticles [57].

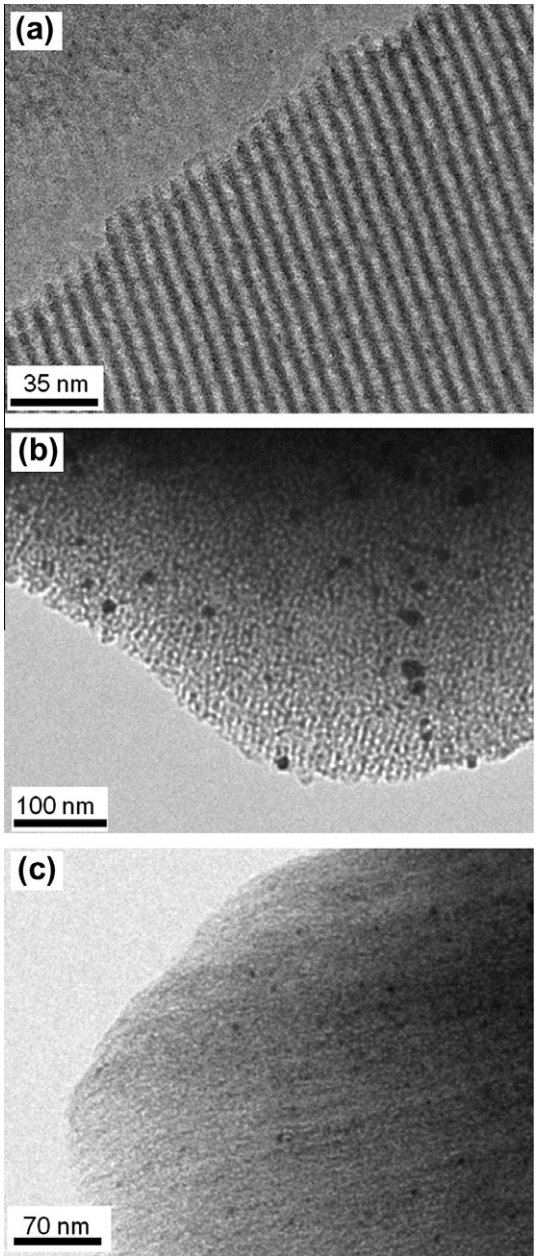

Fig. 4. TEM images of (a) Au–Ti(0.05)-M, (b) Au–Ti(0.05)-P, and (c) Au–Ti(0.05)-N.

Furthermore, the Au–Au coordination numbers (CN_{Au-Au}) for the samples were obtained by fitting (cf. Table 1) and were used to estimate the average sizes of the Au nanoparticles based on face-centered cubic Au structure and a spherical model [41,58]. The Au–Au coordination numbers (6.6–8.3) are very small for

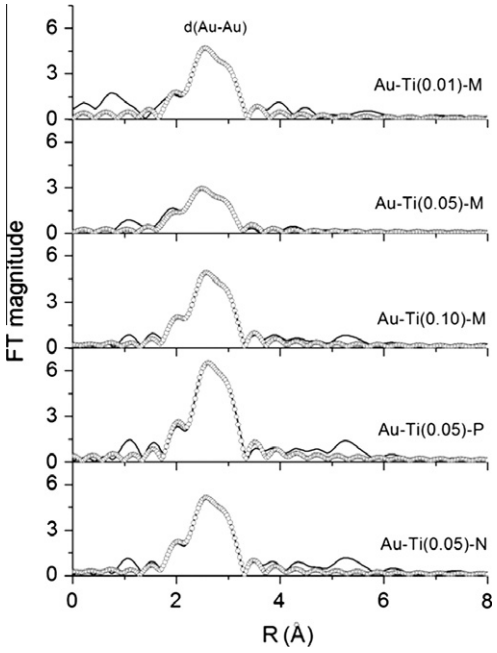

Fig. 5. Fourier transforms of Au L_3-edge k^3-weighted EXAFS data (-) and the fitted results (○), respectively, for the selected Au/TiO_2@SBA-15 samples. Note that the phase shifts were not corrected.

Au–Ti(x)-M, indicative of the small size (1.5–1.8 nm) of the Au nanoparticles in these samples. Au–Ti(0.05)-M showed the smallest Au–Au coordination number and therefore had the smallest Au nanoparticles among all the nanocomposites. For Au–Ti(x)-P and Au–Ti(x)-N samples, the Au–Au coordination numbers are around 9.2–9.7 and the Au particle sizes are estimated to be around 2.5–2.7 nm. The Au particle sizes derived from XAS are smaller than the sizes observed by TEM (cf. Fig. 4). Since EXAFS shows a greater sensitivity toward very small metal nanoparticles (with 100–1200 atoms) than TEM [41], the results may imply that the samples also contain small Au nanoparticles in addition to the relatively large ones observed by TEM.

3.8. Catalytic performance

The Au/TiO_2@SBA-15 materials were applied as catalysts for the direct propylene epoxidation with O_2/H_2, and the results of propylene conversion, hydrogen conversion, PO formation rate, hydrogen efficiency, and product selectivity at different reaction temperatures are summarized in Table 2. The most interesting finding is that besides water, only PO was produced with small amounts of propanal and acetone byproducts from the isomerization of PO. No products involving hydrogenation (propane), cracking/combustion (ethanol and carbon oxides), or oxidation (acrolein) were observed. The product distribution is quite different from that for other mesoporous Au–Ti catalysts under similar reaction conditions [21,39–42,44].

In general, the catalytic performance of most Au/TiO_2@SBA-15 samples is marginally better than the reported Au/Ti-SBA-15 and some other mesoporous silica-based Au–Ti catalysts [40–42], and the catalytic activities increased with increasing reaction temperature. Major differences existed among the catalysts prepared with different surface properties and Ti/Si ratio. For Au–Ti(x)-N, the propylene conversion and the PO formation rate were low and were increased with increasing the TiO_2 loading. On the other hand, an optimum Ti/Si ratio of 0.05 was found for Au–Ti(x)-M and Au–Ti(x)-P in terms of catalytic activity. Au–Ti(0.05)-M is the most active catalyst among all Au/TiO_2@SBA-15 catalysts. It showed higher propylene conversion (2.15%) and higher PO formation rate (51.8 $g_{PO}\ h^{-1}\ kg_{cat}^{-1}$ at 150 °C than the Au/Ti-SBA-15 catalysts (conversions of 0.39–1.1% and PO formation rates of 5.0–16.4 $g_{PO}\ h^{-1}\ kg_{cat}^{-1}$) [41] and the barium-promoted Au/Ti-TUD

Table 2
Overview of the catalytic performances of the Au/TiO_2@SBA-15 samples[a].

Catalyst	T (°C)	C_3H_6 conversion (%)	H_2 conversion (%)	PO formation rate ($g_{PO}\ h^{-1}\ kg_{cat}^{-1}$)	H_2 efficiency (%)	Selectivity (%)		
						PO	Propanal	Acetone
Au–Ti(0.01)-M	80	0.02	0.3	0.8	6.1	>99	0	0
	120	0.04	0.8	1.3	4.1	86	13	1
	150	0.10	1.0	3.8	9.8	97	3	0
Au–Ti(0.05)-M	80	0.44	2.3	17.1	19.1	>99	0	0
	120	1.17	7.3	41.0	14.5	90	3	7
	150	2.15	17.8	51.8	7.5	62	9	29
Au–Ti(0.10)-M	80	0.05	0.9	1.9	5.8	>99	0	0
	120	0.16	1.2	5.6	12.2	90	10	0
	150	0.31	1.8	8.8	12.8	73	24	3
Au–Ti(0.01)-P	80	0.03	0.3	1.2	9.4	>99	0	0
	120	0.10	1.0	3.9	10.5	>99	0	0
	150	0.21	1.5	8.2	14.2	>99	0	0
Au–Ti(0.05)-P	80	0.03	1.2	1.2	2.5	99	1	0
	120	0.27	1.9	9.8	13.5	93	6	1
	150	0.52	3.6	16.8	11.9	83	15	2
Au–Ti(0.10)-P	80	0.07	1.1	2.7	6.4	98	2	0
	120	0.22	1.4	7.9	14.5	92	8	0
	150	0.46	3.0	15.0	13.0	84	15	1
Au–Ti(0.01)-N	80	0.00	0.1	0.0	0.0	0	0	0
	120	0.06	0.2	2.3	3.3	>99	0	0
	150	0.13	1.0	5.1	12.5	>99	0	0
Au–Ti(0.05)-N	80	0.04	11.4	1.6	0.4	>99	0	0
	120	0.14	11.2	5.4	1.3	>99	0	0
	150	0.21	13.0	8.2	1.6	>99	0	0
Au–Ti(0.10)-N	80	0.08	0.6	3.1	12.5	>99	0	0
	120	0.29	1.3	11.3	22.3	>99	0	0
	150	0.47	3.0	16.8	14.6	92	8	0

[a] All the reported values are average values taken from 30–250 min within one epoxidation cycle.

catalysts (conversions of 0.8–2.1% and PO formation rates of 14.4–29.2 $g_{PO}\,h^{-1}\,kg_{cat}^{-1}$) [40]. The PO formation rate at 150 °C is also higher than that (37.2 $g_{PO}\,h^{-1}\,kg_{cat}^{-1}$) for the ammonium-treated Au/Ti-SBA-15 catalyst at 200 °C [42]. However, the PO selectivity of Au–Ti(0.05)-M decreased at high temperatures, accompanied by an increase in the selectivity of acetone. The hydrogen conversion varied considerably among the samples (cf. Table 2). The rate of water formation was found to be between 1.2–214.6 $g_{H2O}\,h^{-1}\,kg_{cat}^{-1}$ depending on the sample. Au–Ti(x)-M and Au–Ti(x)-P generally displayed hydrogen efficiencies in the range of 4.1–19.1%. For Au–Ti(x)-N, the highest hydrogen efficiency was found for the sample prepared at Ti/Si = 0.10.

3.9. Catalyst stability

The Au/TiO_2@SBA-15 samples exhibited stable catalytic performance. Fig. 6 shows the changes in propylene conversion, PO selectivity, and hydrogen conversion with time on stream for the selected samples at 150 °C. For all the samples, the propylene conversion increased within the first 5–10 min and then leveled off for the remaining on-stream time. Au–Ti(0.05)-M exhibited the highest conversion. Similar trends were observed in PO selectivity and hydrogen efficiency for all the catalysts except Au–Ti(0.05)-M, for which both the PO selectivity and hydrogen efficiency decreased within the first hour of the reaction and thereafter reached relatively constant values.

Fig. 7 compares the PO formation rates for the catalysts at on-stream times of 5, 30, and 250 min at three different reaction temperatures. At 80 °C, only Au–Ti(0.05)-M produced some PO. The PO formation rate slightly increased from 22.8 $g_{PO}\,h^{-1}\,kg_{cat}^{-1}$ at 5 min to 24.9 $g_{PO}\,h^{-1}\,kg_{cat}^{-1}$ at 30 min and then gradually decreased to at 15.1 $g_{PO}\,h^{-1}\,kg_{cat}^{-1}$ at 250 min, corresponding to a decrease of ~39% as compared to the value at 30 min. At 120 °C, Au–Ti(0.05)-M exhibited increased PO formation rate while the other catalysts except Au–Ti(0.01)-M started to produce PO at rates between 5–10 $g_{PO}\,h^{-1}\,kg_{cat}^{-1}$. For Au–Ti(0.05)-M, a decrease of 28% was observed by comparison of the maximum activity with that after 250 min. When the reaction temperature was increased to 150 °C, Au-Ti(0.05)-N exhibited a very stable PO formation with rates of 8.1–8.4 $g_{PO}\,h^{-1}\,kg_{cat}^{-1}$ over around 4 h. On the other hand, the PO formation rates of the Au–Ti(x)-M and Au–Ti(x)-P peaked at around 30 min and then slightly decreased during the following period of time. By comparing values at 30 and 250 min, Au–Ti(0.05)-M showed a decrease of 19%, while the activities for other catalysts decreased by about 1.6–2.9%. Compared to other mesoporous Au–Ti catalysts [21,39–42,44], the Au/TiO_2@SBA-15 catalysts are more stable during the propylene epoxidation reaction at relatively low (⩽150 °C) temperature.

The most active Au–Ti(0.05)-M was tested in successive cycles including an intermediate regeneration in O_2/He at 300 °C, and a decrease of ~8% in the PO formation rate at 150 °C was observed (see Fig. S5 in the Supporting Material). The same catalyst from different batches was also tested at 150 °C, and almost the same catalytic activity was found (see Fig. S5 in the Supporting Material).

3.10. Relation between catalyst structure and catalytic performance

As revealed in the characterization results, the Au/TiO_2@SBA-15 materials possess different structures as compared to the earlier reported mesoporous Au-Ti catalysts. The TiO_2 nanophases confined in the micropores of SBA-15 were formed after a thermal treatment at 350 °C, a temperature at which the amorphous TiO_2 is possibly transformed to anatase [59]. Accordingly, these nanophases may either be totally amorphous or contain some anatase nanocrystals that were too small to be detected by XRD. The presence of TMS or TPS groups also influenced the subsequent deposition of Au nanoparticles. For the silica-supported TiO_2 materials, as in the cases of Ti(x)-N samples, the preferential deposition of negatively charged Au salts on mixed SiO_2/TiO_2 is mainly dictated by the difference in the isoelectric points of silica (~2) and TiO_2 (~6–8, structure-dependent) [60]. If the silica surface was passivated by TMS or TPS groups, the Au salts could only adsorb on the TiO_2 nanophases, resulting in a better control over the position of Au deposition. As a result, almost all the Au/TiO_2@SBA-15 samples have fully open mesopores after the subsequent deposition of TiO_2 and Au. The exceptions are Au–Ti(x)-P with the higher Au loading and larger Au nanoparticles, for which the TPS groups are likely to interact with Au^{3+} and stabilize the reduced $Au^{(0)}$.

Regarding the catalytic performance for propylene epoxidation with O_2/H_2, Au/TiO_2@SBA-15 showed slightly better but more stable activities and only generated PO, propanal, acetone, and water. As mentioned above, Haruta et al. have shown that Au nanoparticles smaller than 2 nm are quite active in the hydrogenation of propylene and those between 2 and 5 nm are preferred for the epoxidation of propylene to PO [15]. However, propane was not

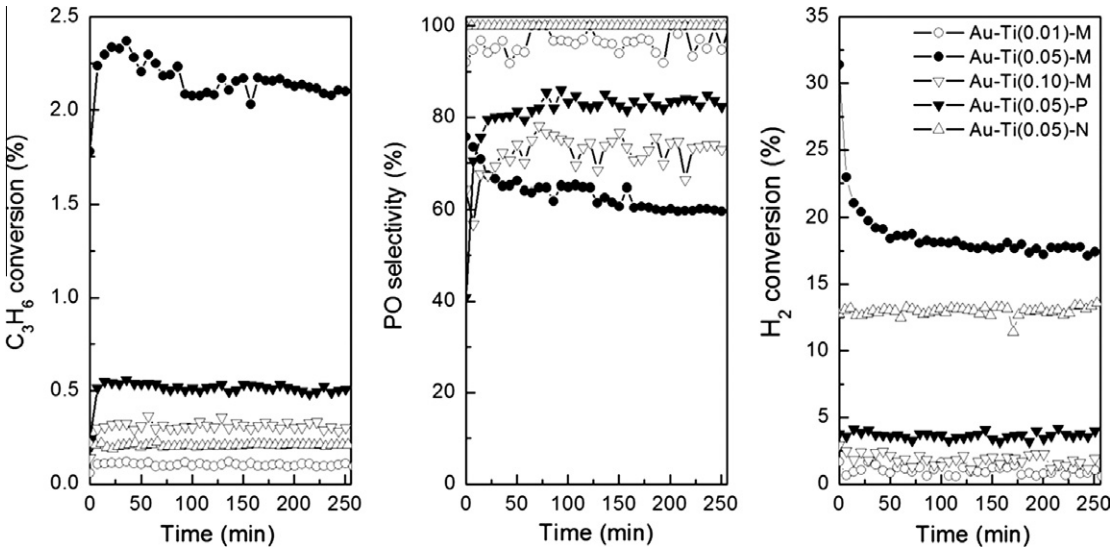

Fig. 6. Changes in propene conversion, PO selectivity, and H_2 conversion with on-stream time for the selected Au/TiO_2@SBA-15 catalysts at 150 °C.

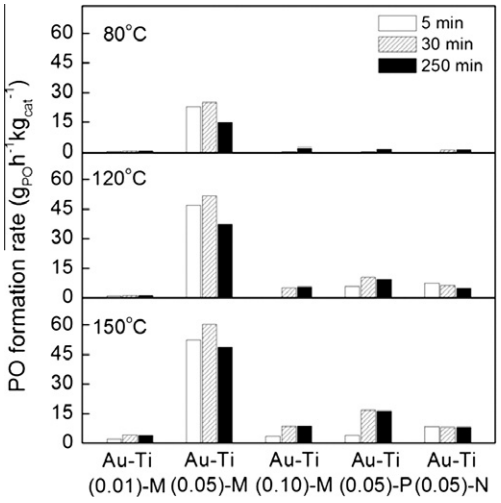

Fig. 7. Comparison of PO formation rates for the selected Au/TiO_2@SBA-15 catalysts at different on-stream time at 80 °C, 120 °C, and 150 °C.

found in the product mixture for any of the Au/TiO_2@SBA-15 catalysts. Au–Ti(0.05)-M with the smallest Au nanoparticles (~1.5 nm) exhibited comparatively high propylene conversions and PO formation rates without producing propane. The reproducibility of the results was also verified (cf. Fig. S5 in the Supporting Material). The TS-1-supported Au catalysts reported by Delgass et al. also contained very small Au clusters (<2 nm) [26]. The Au/TS-1 catalysts are highly active and stable at 140–200 °C, but they produced cracking products (ethanal and CO_2) and became less active than Au/TiO_2 catalysts at low temperature [26]. Therefore, in addition to the size of Au nanoparticles, there exist other factors influencing the catalytic performance of Au/TiO_2@SBA-15 catalysts.

The nature of the titanium species was also considered. Most of the mesoporous silica-supported Au–Ti catalysts contained predominantly tetrahedral-coordinated titanium species on the surface, and the reactions over these catalysts often produced byproducts involving isomerization and cracking. Haruta et al. found that these byproducts were formed from the consecutive reactions of PO [22]. The kinetic study by Oyama et al. showed that the formation of CO_2 was closely related to the concentration of PO and not to that of propylene [61]. On the other hand, the Au catalysts supported on P25 or anatase TiO_2 gave similar product distribution with those for the Au/TiO_2@SBA-15 catalysts at low reaction temperatures [15,29]. Since the TiO_2 nanophases in Au/TiO_2@SBA-15 were "aggregated" in the micropores instead of dispersed on the mesopore surface, it is reasonable to compare them to P25- or anatase-supported catalysts. However, those Au/TiO_2 catalysts suffered from fast deactivation and low PO yields and generated CO_2 as the major product at a temperature higher than 100 °C [15,29]. As compared to them, the improved activity and stability of Au/TiO_2@SBA-15 seem to be associated with the confinement of the TiO_2 phases, with the optimum amount (x = 0.05 for Au–Ti(x)-M and Au–Ti(x)-P), in the micropores and probably also to the hydrophobicity of the mesopores. With Au nanoparticles deposited on the confined TiO_2 nanophases, the number of Ti sites at the periphery of Au nanoparticles would be limited. As a result, it would be more difficult for PO to be readsorbed and further reacted to CO_2 or other species to deactivate the catalyst. For Au–Ti(0.05)-M, its high catalytic activity is therefore most likely attributed to the very small size of Au deposited on the TiO_2 nanophases. The fully open and hydrophobic mesopores would also contribute to the high activity, because the PO product can diffuse fast from the catalytic sites without being further converted.

4. Conclusion

A new type of Au/TiO_2@SBA-15 catalysts has been designed and prepared. TiO_2 was incorporated selectively in the micropores of SBA-15, and small Au nanoparticles were deposited on top of the TiO_2 nanophases. The catalysts had highly ordered hexagonal mesostructure, and most of them had fully open mesopores grafted with residual TMS or TPS groups. They showed highly stable catalytic activities for the direct propylene epoxidation with O_2/H_2 and produced propanal and acetone as the only byproducts in addition to PO. Among all the samples studied, Au–Ti(0.05)-M containing 1.5-nm Au nanoparticles was found to be the best catalyst and it outperformed Au/Ti-SBA-15 and some other mesoporous Au–Ti catalysts reported in literature. The unique and improved catalytic behavior is related to the unique structure of very small Au nanoparticles on nanosized TiO_2 phases located in the micropores and the hydrophobicity of the fully open mesopores, which avoids further conversion of PO.

Acknowledgement

This research has been carried out in the NWO-NSC program between the Netherlands Organization for Scientific Research and the National Science Council of Taiwan (NSC 95-2911-I-007-030). C.H.L and C.M.Y. thank Dr. Ting-Shan Chan and Cheng-An Hsieh for their help on XAS measurements. E.H. thanks the Technology Foundation STW and the Applied Science Division of NWO for support. E.H. and Y.G. also acknowledge support of the Royal Netherlands Academy of Arts and Science and the Chinese Ministry of Science and Technology.

Appendix A. Supplementary material

Supplementary data associated with this article can be found, in the online version, at doi:10.1016/j.jcat.2011.06.001.

References

[1] D.L. Trent, Kirk-Othmer Encyclopedia of Chemical Technology, Wiley, New York, 1996.
[2] K. Weissermel, H.J. Arpe, Industrial Organic Chemistry, second ed., VCH, New York, 1993.
[3] M. Mccoy, C.E.N.N. Bureau, Chem. Eng. News 79 (2001) 19.
[4] A. Tullo, Chem. Eng. News 82 (2004) 15.
[5] A. Tullo, Chem. Eng. News 83 (2005) 7.
[6] A.H. Tullo, P.L. Short, Chem. Eng. News 84 (2006) 22.
[7] M. Akimoto, K. Ichikawa, E. Echigoya, J. Catal. 76 (1982) 333.
[8] M.A. Barteau, R.J. Madix, J. Am. Chem. Soc. 105 (1983) 344.
[9] J. Lu, J.J. Bravo-Suáez, A. Takahashi, M. Haruta, S.T. Oyama, J. Catal. 232 (2005) 85.
[10] D. Sullivan, P. Hooks, M. Mier, J. van Hal, X. Zhang, Top. Catal. 38 (2006) 303.
[11] J. Lu, M. Luo, H. Lei, C. Li, Appl. Catal. A: Gen. 237 (2002) 11.
[12] G. Lu, X. Zuo, Catal. Lett. 58 (1999) 67.
[13] O.P.H. Vaughan, G. Kyriakou, N. Macleod, M. Tikhov, R.M. Lambert, J. Catal. 236 (2005) 401.
[14] H. Chu, L.u. Yang, Q. Zhang, Y. Wang, J. Catal. 241 (2006) 225.
[15] T. Hayashi, K. Tanaka, M. Haruta, J. Catal. 178 (1998) 566.
[16] M. Haruta, CATTECH 6 (2002) 102.
[17] T.A. Nijhuis, M. Makkee, J.A. Moulijn, B.M. Weckhuysen, Ind. Eng. Chem. Res. 45 (2006) 3447.
[18] B.K. Min, C.M. Friend, Chem. Rev. 107 (2007) 2709.
[19] C.X. Qi, Gold Bull. 41 (2008) 224.
[20] M. Haruta, Nature 437 (2005) 1098.
[21] B.S. Uphade, T. Akita, T. Nakamura, M. Haruta, J. Catal. 209 (2002) 331.
[22] A.K. Sinha, S. Seelan, T. Akita, S. Tsubota, M. Haruta, Appl. Catal. A: Gen. 240 (2003) 243.
[23] J. Lu, X. Zhang, J.J. Bravo-Suáez, T. Fujitani, S.T. Oyama, Catal. Today 147 (2009) 186.
[24] M. Haruta, N. Yamada, T. Kobayashi, S. Iijima, J. Catal. 115 (1989) 301.
[25] T.A. Nijhuis, T. Visser, B.M. Weckhuysen, J. Phys. Chem. B 109 (2005) 19309.

[26] B. Taylor, J. Lauterbach, W.N. Delgass, Appl. Catal. A: Gen. 291 (2005) 188.
[27] C. Sivadinarayana, T.V. Choudhary, L.L. Daemen, J. Eckert, D.W. Goodman, J. Am. Chem. Soc. 126 (2003) 38.
[28] P. Landon, P.J. Collier, A.J. Papworth, C.J. Kiely, G.J. Hutchings, Chem. Commun. (2002) 2058.
[29] M. Haruta, B.S. Uphade, S. Tsubota, A. Miyamoto, Res. Chem. Intermed. 24 (1998) 329.
[30] T.A. Nijhuis, T.Q. Gardner, B.M. Weckhuysen, J. Catal. 236 (2005) 153.
[31] W.T. Wallace, D.W. Goodman, J. Phys. Chem. B 108 (2004) 14609.
[32] L. Giordano, A. Del Vitto, G. Pacchioni, J. Chem. Phys. 124 (2006) 134701.
[33] G. Mul, A. Zwijnenburg, B. van der Linden, M. Makkee, J.A. Moulijn, J. Catal. 201 (2001) 128.
[34] T.A. Nijhuis, B.J. Huizinga, M. Makkee, J.A. Moulijn, Ind. Eng. Chem. Res. 38 (1999) 884.
[35] B. Taylor, R.P. Andres, W.N. Delgass, J. Phys. Chem. B 109 (2004) 2321.
[36] A. Ruiz, B. van der Linden, M. Makkee, G. Mul, J. Catal. 266 (2009) 286.
[37] U. Ciesla, F. Schüth, Micropor. Mesopor. Mater. 27 (1999) 131.
[38] Y.A. Kalvachev, T. Hayashi, S. Tsubota, M. Haruta, J. Catal. 186 (1999) 228.
[39] B.S. Uphade, Y. Yamada, T. Akita, T. Nakamura, M. Haruta, Appl. Catal. A: Gen. 215 (2001) 137.
[40] J. Lu, X. Zhang, J.J. Bravo-Suáez, K.K. Bando, T. Fujitani, S.T. Oyama, J. Catal. 250 (2007) 350.
[41] E. Sacaliuc, A.M. Beale, B.M. Weckhuysen, T.A. Nijhuis, J. Catal. 248 (2007) 235.
[42] E. Sacaliuc-Parvulescu, H. Friedrich, R. Palkovits, B.M. Weckhuysen, T.A. Nijhuis, J. Catal. 259 (2008) 43.
[43] T.A. Nijhuis, E. Sacaliuc-Parvulescu, N.S. Govender, J.C. Schouten, B.M. Weckhuysen, J. Catal. 265 (2009) 161.
[44] A.K. Sinha, S. Seelan, S. Tsubota, M. Haruta, Angew. Chem. Int. Ed. 43 (2004) 1546.
[45] T.A. Nijhuis, B.M. Weckhuysen, Chem. Commun. (2005) 6002.
[46] D.Y. Zhao, J.L. Feng, Q.S. Huo, N. Melosh, G.H. Fredrickson, B.F. Chmelka, G.D. Stucky, Science 279 (1998) 548.
[47] A. Galarneau, H. Cambon, F. Di Renzo, R. Ryoo, M. Choi, F. Fajula, New J. Chem. 27 (2003) 73.
[48] C.-M. Yang, H.-A. Lin, B. Zibrowius, B. Spliethoff, F. Schüth, S.-C. Liou, M.-W. Chu, C.-H. Chen, Chem. Mater. 19 (2007) 3205.
[49] H.-A. Lin, C.-H. Liu, W.-C. Huang, S.-C. Liou, M.-W. Chu, C.-H. Chen, J.-F. Lee, C.-M. Yang, Chem. Mater. 20 (2008) 6617.
[50] C.-M. Yang, B. Zibrowius, W. Schmidt, F. Schüth, Chem. Mater. 15 (2003) 3739.
[51] C.-M. Yang, B. Zibrowius, W. Schmidt, F. Schüth, Chem. Mater. 16 (2004) 2918.
[52] W.-Y. Yu, C.-P. Yang, J.-N. Lin, C.-N. Kuo, B.-Z. Wan, Chem. Commun. (2005) 354.
[53] T. Maddanimath, A. Kumar, J. D'Arcy-Gall, P.G. Ganesan, K. Vijayamohanan, G. Ramanath, Chem. Commun. (2005) 1435.
[54] H. Miyamura, R. Matsubara, Y. Miyazaki, S. Kobayashi, Angew. Chem. Int. Ed. 46 (2007) 4151.
[55] J.M. Thomas, G. Sankar, Acc. Chem. Res. 34 (2001) 571.
[56] A. Hagen, K. Schueler, F. Roessner, Micropor. Mesopor. Mater. 51 (2002) 23.
[57] B. Delley, D.E. Ellis, A.J. Freeman, E.J. Baerends, D. Post, Phys. Rev. B 27 (1983) 2132.
[58] A. Jentys, PCCP 1 (1999) 4059.
[59] E.L. Crepaldi, G.J.d.A.A. Soler-Illia, D. Grosso, F. Cagnol, F. Ribot, C. Sanchez, J. Am. Chem. Soc. 125 (2003) 9770.
[60] C.J. Brinker, G.W. Scherer, Sol–Gel Science 1990.
[61] J. Lu, X. Zhang, J.J. Bravo-Suáez, S. Tsubota, J. Gaudet, S.T. Oyama, Catal. Today 123 (2007) 189.